



# Millimeter-sized piezoelectric flextensional actuators with improved mechanical efficiency

P. York<sup>a,b,\*</sup>, N. Jafferis<sup>a,b</sup>, R. Wood<sup>a,b</sup>

<sup>a</sup> Harvard University, John A. Paulsen School of Engineering and Applied Sciences, 60 Oxford Street, Cambridge, MA 02138, United States

<sup>b</sup> Wyss Institute for Biologically-Inspired Engineering, 3 Blackfan Circle, Boston, MA 02115, United States



## ARTICLE INFO

### Article history:

Received 13 December 2019  
Received in revised form 5 May 2020  
Accepted 12 May 2020  
Available online 19 May 2020

### Keywords:

Piezoelectric actuators  
Compliant mechanisms  
Micromachining  
Composite structures

## ABSTRACT

A millimeter-sized piezoelectric actuator with a flexible displacement-amplification frame incorporates design enhancements to achieve an increase in mechanical efficiency from 33 to 70% relative to existing designs. The basic insight enabling this improvement is a familiar one: to maximize the force transfer through a flexible transmission, the serial compliance of the transmission should be minimized. The execution is more complex, particularly due to the small size of the actuators, requiring careful material selection, design, and fabrication. We provide simple guidelines based on lumped parameter modeling and scaling analysis to assist designers in this challenging task and in customizing to specific size and output requirements. These actuators can be used as building blocks in millimeter-sized devices in which precise, linear motion is needed, and the method of analysis employed should be broadly useful to designers of similar devices looking to distill a complex mechanics problem down to a set of simple design guidelines.

© 2020 Elsevier B.V. All rights reserved.

## 1. Introduction

In “flextensional” piezoelectric actuators, the large tensile stresses generated via the converse piezoelectric effect ( $\sim 25 \text{ Pa V}^{-1}$ ) induce small displacements ( $\sim 0.1\%$  strain) which are transformed through a flexible linkage into a larger displacement at the expense of output force. The term “flextensional” originated with the use of amplified piezoelectric actuators in sonar applications, as described in [1], and can be used as an umbrella term for piezoelectric actuators with displacement amplified through a compliant frame.

For this class of actuators, the piezoelectric element would ideally be able to deliver all of its energy to the output, but in practice this is difficult to achieve because of internal deformation of the structure: links are not completely rigid and flexures are not ideal pin joints. The quality of this conversion is termed “mechanical efficiency”, which represents the reduction in work output of the actuator from that of the active element. Similarly, the ideal flexible linkage would have negligible mass relative to the active material. In practice, the non-negligible mass of the linkage is dead weight that does not contribute to energy conversion. This sug-

gests another quality metric, “mass efficiency”, the ratio of the piezoelectric element mass to the total mass of the actuator.

Mechanical and mass efficiency are useful concepts because together they describe the quality of an actuator design as a function of the geometry and material selection. They are more fundamental than quantities such as absolute output force, displacement, or bandwidth, which represent the performance of a specific design configuration (e.g., dimensions). For an ideal design, quality would be insensitive to configuration, but in reality, some dependence of quality on configuration will likely occur.

Together, mass and mechanical efficiency describe the reduction in energy density from that of the active material. A key goal of actuator design is often to maximize energy density [2]. Micro-robotic systems such as those of Jafferis et al. [3] and Yang et al. [4] have severe mass and energy budgets – in those examples, every micro Joule of actuation energy counts toward greater in-flight capabilities, and every additional milligram of weight counts against longer flight times and sensory payload. Energy density is similarly important in aerospace and satellite deployments and in active-damping applications, in which minimal passive inertia is desired. Considering actuator energy density in terms of mass and mechanical efficiency makes plain the options to increase it: reduce passive mass, better match active element and amplification frame stiffnesses, or use a more energetic active material. It also makes clear the upper bound on actuator energy density for which to aim – the full energy density of the active material.

\* Corresponding author at: Harvard University, John A. Paulsen School of Engineering and Applied Sciences, 60 Oxford Street, Cambridge, MA 02138, United States.  
E-mail address: [pyork@g.harvard.edu](mailto:pyork@g.harvard.edu) (P. York).

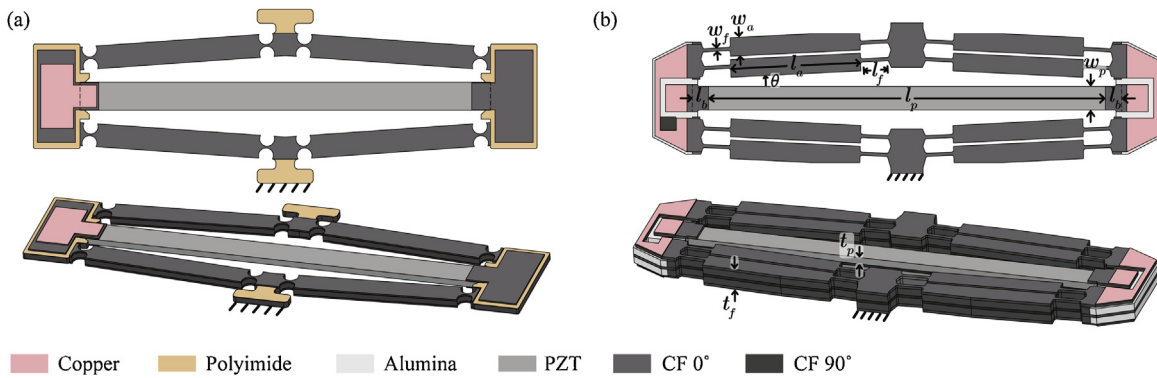


**Fig. 1.** (a) Prior design, with a single piezoelectric element and a unidirectional carbon fiber frame that is insulated from the piezoceramic using a thin parylene coating. (b) Improved design, with two piezoceramic elements and an alumina-reinforced frame for more efficient force transfer. The parallelogram structure further reduces serial compliance in addition to inhibiting off-axis translation and rotation, which can arise from external disturbances or structural asymmetries.

The contribution of this work is to show how to design and fabricate flextensional piezoelectric actuators on the millimeter scale with similar mechanical and mass efficiency at high transmission ratios to their centimeter-scale counterparts. In doing so, we aim to both enable new millimeter-scale systems and to facilitate the downscaling of existing centimeter-sized devices. The potential applications for these devices on the millimeter scale are numerous, as judged by existing deployments in centimeter-sized systems. Claeysen et al. [5], describe a host of device applications: micro-scanning and shutter control for high-speed optical systems, active damping and shape control in aerodynamic systems, and acoustic sourcing for mapping underwater pipe networks and structural health monitoring. Janker et al. [6] describe a wing morphing mechanism and vibration absorbers for helicopters and automobiles. Zubir et al. [7] incorporate a modified flextensional actuator into a microgripping tool. Feenstra et al. [8] demonstrate a proof of concept device using the flexible frame to couple a piezoelectric stack to the vibrations of a backpack. Liu et al. [9] and Lee et al. [10] use flextensional actuators as the basis for in-plane and out-of-plane micropositioning stages, respectively.

The actuators described herein build on previously reported efforts [11] toward the fabrication of high-performing flextensional piezoelectric actuators on the millimeter scale. Design improvements that increase the actuator's mechanical efficiency from 33% to 70% across multiple design generations are described in detail in Section 2. Core to this advancement is the incorporation of alumina base connections between the linkage frame and the piezoceramic transducer. This required significant modification of previously described fabrication techniques. The new process is presented in Section 3. Secondary are modeling efforts that employ lumped parameter modeling and scaling analysis to facilitate the derivation of design guidelines for proper selection of critical geometric parameters. Finally, the results of the design enhancements are shown in Section 5, and a comparison to bimorph bending actuators, limitations to the described approach, and avenues for further improvement are discussed in Section 6.

## 2. Design improvements

Three key design improvements contribute to improved performance and manufacturability relative to previous versions of these devices: (1) the incorporation of high-modulus alumina to create a stiff connection between the piezoceramics and the amplification frame, (2) the use of a parallelogram linkage structure to improve the off-axis stiffness at no expense to on-axis performance, and (3) the addition of a second layer of piezoceramic, which reduces out-of-plane motion and allows the fabrication process to be modified in advantageous ways. These differences are illustrated in Fig. 1,

in which the prior design and current version are shown. Each design improvement is described in detail below, with a focus on the performance benefits accrued and the implications for device fabrication of each modification.

### 2.1. Alumina base connections

In the prior actuator design, the entire frame around the piezoceramic element was made from unidirectional carbon fiber. This had the advantage of minimizing the number of parts needed while ensuring that the flexures and linkage arms were stiff along their length, i.e., in the direction of force transmission. However, unidirectional fibers have a key structural deficiency: they are weak in shear in the planes parallel to the fibers. This was an issue in the regions of the actuator connecting the piezoceramic to the flexure transmission. When the output link of the actuator was blocked, these regions could not resist the shear stresses that arose due to the contractile force of the piezoceramic.

In the improved design, the shear stiffness in the key connecting regions is increased by  $\sim 30\times$  by replacing the unidirectional carbon fiber laminate ( $G = 5$  GPa) with alumina ( $G = 150$  GPa). Finite element analysis, conducted in COMSOL 5.0 and shown in Fig. 2, indicates that this yields an increase in blocked force of 40%, at the cost of a 9% increase in mass. Alumina is heavier than carbon fiber ( $3.9$  g/cm<sup>3</sup> vs.  $1.6$  g/cm<sup>3</sup>), but it only represents a small fraction (15%) of the total actuator mass.

A few details regarding the finite element analysis should be mentioned. Because of symmetry, only one quarter of the device needs to be simulated. Thus, we employ symmetry boundary conditions on the medial edges of the piezoceramic element and the medial edge of the output link. Another simplification we made was treating the piezoceramic element as a force source applying a boundary force to the compliant frame. For meshing, we used triangular elements using COMSOL's "extremely fine physics-controlled mesh", which generated a minimum element quality of 0.71, on a scale of 0 to 1. Within COMSOL, a minimum element quality greater than 0.1 indicates that a mesh is acceptably scaled and reasonably captures the underlying geometry. The study does not include geometric nonlinearities. We anticipate that the effect of considering geometric nonlinearities would not dramatically alter the simulation results, because the displacements are small, and moreover, any errors from assuming geometric linearity will be similarly felt between the different designs under comparison. This is important because the aim of the study is to compare different design choices and not necessarily the absolute prediction of performance.

Creating the composite alumina/carbon fiber frame also necessitated some rethinking of the fabrication processes. Previously, the carbon fiber frames were pre-machined and the piezoceramic ele-

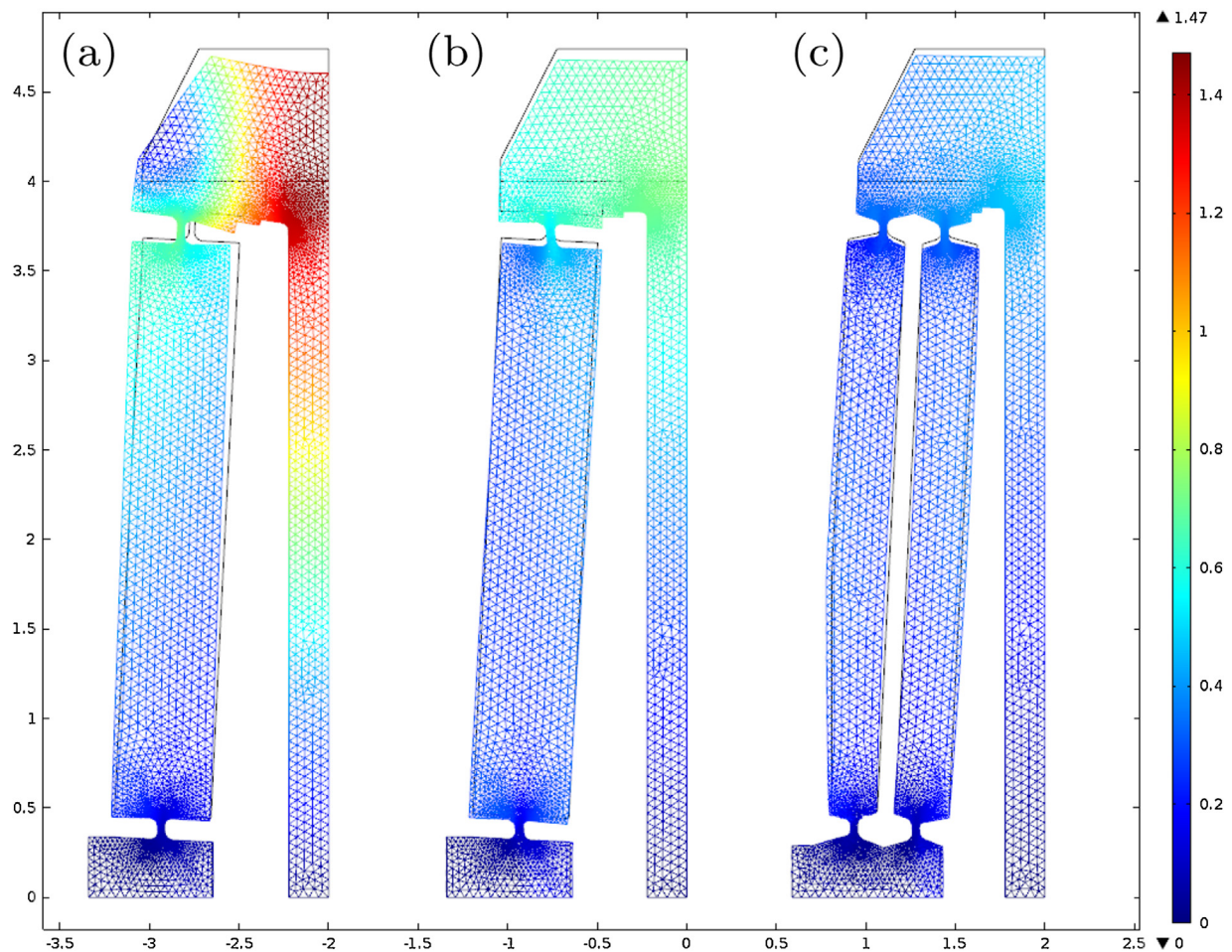


**Fig. 2.** Finite element models showing the internal deformation with the output link blocked for three different actuator designs: (a) carbon fiber frame, (b) alumina-reinforced frame, and (c) alumina-reinforced frame with parallelogram amplification linkage. The unit of displacement is  $\mu\text{m}$  and deformation is scaled by  $100\times$ . The alumina-reinforced design experiences 40% less deformation at the piezoceramic/frame boundary than the carbon fiber design, and the parallelogram design sees 15% less deformation than the single-arm design. This fraction is the same by which the blocked force at the output link is increased.

ments placed inside before lamination. This is a somewhat fraught process, because nothing holds the piezoceramics in place during the lamination. This issue would be exacerbated by the need to also place alumina pieces inside the frame; moreover, this manual placement process is time sensitive, because prepreg carbon fiber desiccates and begins to cure out at room temperature, leading to inadequate interlayer bonding.

## 2.2. Double layer of PZT

To surmount these fabrication challenges, we added a second piezoceramic layer, which meant that the piezoceramic/alumina connection would no longer occur in the center plane of the laminate. This allowed the pieces of piezoceramic, alumina, and carbon fiber to be held in place by carrier layers (Gel-Pak) and laminated together using the prepreg carbon fiber that becomes the center layer of the laminate. This approach is inspired by the fabrication process for bimorph bending actuators presented in [12]. It is described in more detail below in Section 3.

Adding the second layer of piezoceramic roughly doubles the thickness of the device, which could be detrimental in the most space-constrained applications, but other benefits beyond manufacturability are accrued. During laser micromachining, a small taper on each edge is introduced. This variation in edge thickness results in a net moment being generated by the piezoceramic in addition to its contractile force. For the previous actuator design,

this moment created an out-of-plane motion of the piezoceramic and resulted in out-of-plane motion of the output link on the order of a few percent of the in-plane motion. In the new design, by essentially stacking two of the previous actuators back-to-back, the moments cancel and the out-of-plane motion is eliminated.

Increasing the thickness of the actuator also clearly increases the off-axis stiffness at the output link in the out-of-plane direction. This could be advantageous if the load being driven is not well supported or is subject to external disturbances. A final, more speculative benefit is that by reducing out-of-plane motion, actuator lifetime at high voltages will be increased. The primary mechanical failure mode of piezoceramics is crack propagation initiated by tensile strain, and the parasitic out-of-plane bending implies some small tensile strain that could lead to premature failure of the device.

## 2.3. Parallelogram arm structure

The use of a parallelogram structure is not unique to this work, having been described previously by [13,14] among others. This structure is used here because it improves the output properties of the actuator, in both a static and dynamic sense. It is significantly stiffer than the single-arm approach in off-axis directions, particularly in the in-plane direction lateral to the output motion. Finite element analysis indicates an increase of  $\sim 20\times$  in stiffness in this direction relative to the non-parallelogram design. The increase in

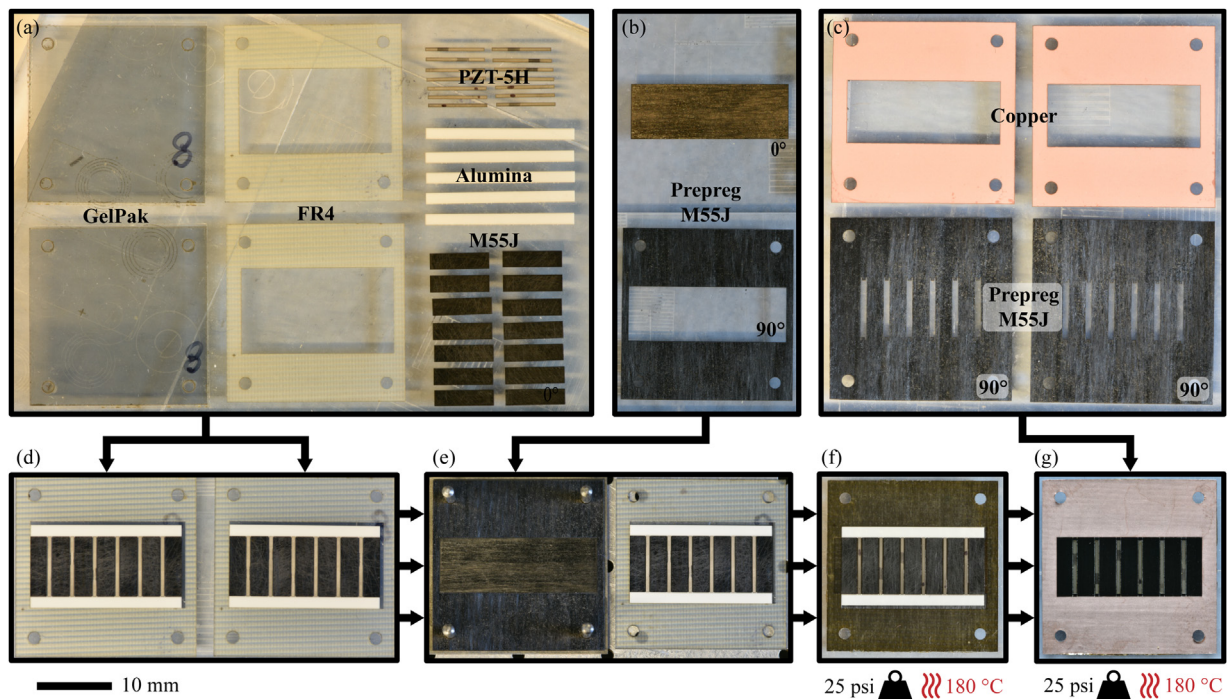


**Fig. 3.** The flextensional actuators are formed from a piezoceramic/carbon-fiber/alumina laminated composite. The arrows show the process flow from the forming of raw materials (a–c) to assembly and lamination (d–g). Heat and pressure are applied in assembly steps (f) and (g). The composite thus formed contains six actuators ready to be released from the substrate.

off-axis stiffness also implies improved disturbance rejection and attenuation of unwanted dynamic modes.

The manufacturing process for making the parallelogram structure is little changed from that of the single arm design. Some care must be taken for chip removal in the small internal regions between the flexures, but this is generally achievable through the appropriate selection of processing parameters. The gap between the two arms of the parallelogram structure should be small enough to permit movement, but too much clearance will result in reduced stiffness of the linkage arms, assuming the total area available for the structure is fixed. In this work we took a somewhat conservative approach and oversized the gap to make the fabrication process easier, but some small performance increase could likely be gained by reducing the gap size closer to the kinematic limit.

### 3. Manufacturing

The actuator fabrication proceeds in three broad steps: lamination of the constituent materials, laser micromachining to create the actuator structure and release it from the laminate, and post-processing, which includes cleaning, dielectric breakdown enhancement, and wiring. The process easily lends itself to batch fabrication; only the post-processing steps require individualized handling and manipulation of the actuators.

The goal of the lamination step, shown in Fig. 3, is to create strong inter-layer bonds while ensuring good lateral alignment between layers. The first two layers are formed from individual pieces of PZT-5H, as-fired alumina, and cured unidirectional M55J carbon fiber (a). The carbon fiber pieces are sanded to match the thickness of the PZT-5H and alumina ( $135\ \mu\text{m}$ ). The pieces are placed into the FR4 alignment frames and held in place by a gel carrier (GelPak x8, Delphon Industries). Small notches in the alumina allow the carbon fiber and piezoceramic pieces to be laterally aligned. Vertical alignment puts the piezoceramic and alumina pieces in direct contact, leaving a small gap in the vertical direction between the alumina and the carbon fiber pieces. The center

layer (b), an adhesive layer, is formed from two pieces of prepreg M55J/RS-3C carbon fiber composite. The outer piece has its fibers aligned along the length of the actuator, to ensure strong mechanical connection between the piezoceramic and alumina and a low resistance electrical connection to the inner piezoceramic layers, and the inner piece has its fibers aligned perpendicularly to the actuator length, so as not to inhibit the piezo-induced motion. The outer layers (c), are made from prepreg M55J/RS-3C and a two-layered copper. The carbon fiber provides mechanical and electrical connection to the piezoceramic, and the copper allows for easy electrical connection to external drive electronics. The assembly process is shown in (d–g); first, the FR4-held pieces are bonded to either side of the center layer (d–f), then the GelPak is peeled off and the outer layers are bonded on (g). During this lamination, a chemically-resistant layer (FEP) and conformable layer (Paco-Pad) are used to ensure uniform pressure throughout the stack and are then discarded after the lamination. A pressure of 25 psi and the manufacturer-recommended temperature profile were used for both laminations.

There are a few subtle points of this lamination process that bear mentioning. First, all of the constituent materials are cut using a 355-nm 7-W pulsed laser (Coherent Avia 355-7). Because of the finite depth of field of the focusing optics, each piece has a tapered edge with taper width approximately equal to 1/10th of the thickness. Not keeping track of this taper can lead to poor lateral alignment and weak mechanical connection between the alumina and the piezoceramic. To avoid this, we keep track of the taper direction and proceed with the assembly shown in (d) to align the tapers of adjacent pieces so as to minimize the air gap between them. The use of laser micromachining also necessitates some amount of tedious cleaning; we clean each piece of piezoceramic after cutting (Fig. 3a) with isopropyl alcohol using a small fabric wipe so as to remove any debris deposited on the edges. This prevents premature dielectric breakdown of the piezoceramic. Second, the use of as-fired alumina, rather than polished, and the use of sanded M55J is important to ensure strong bonding with the

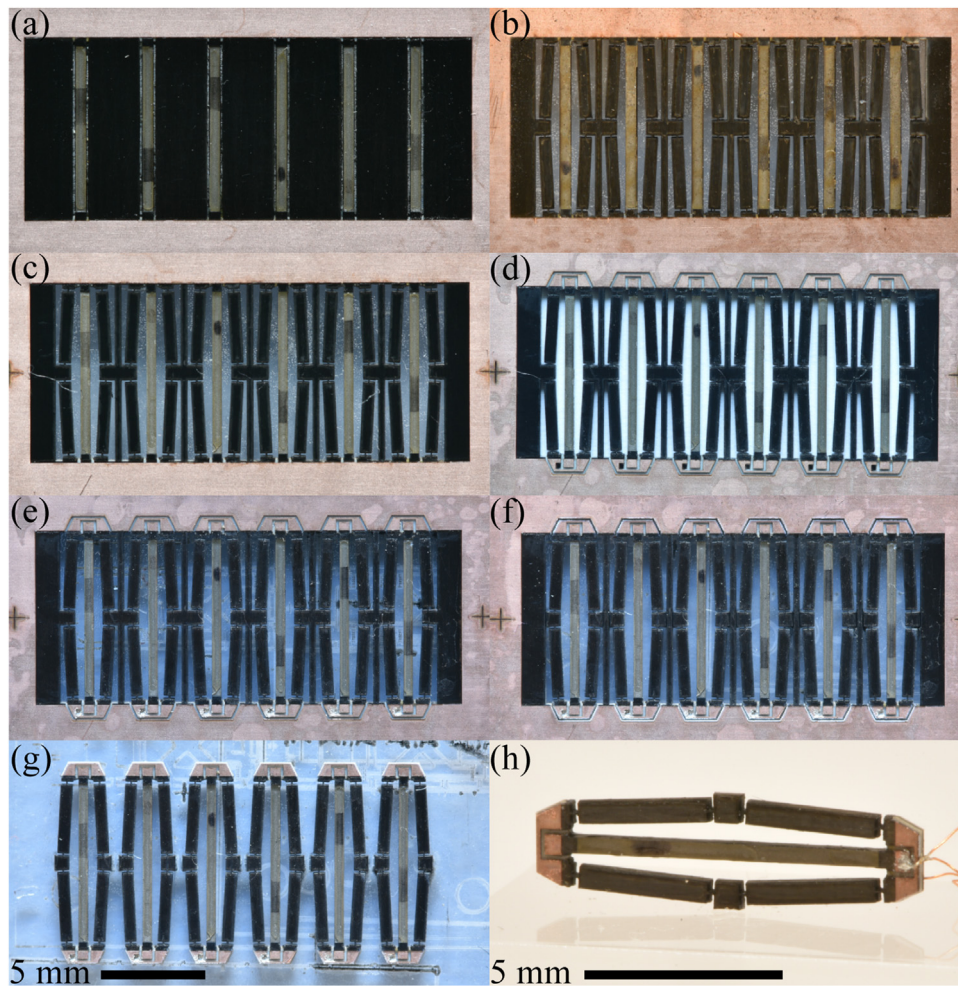


**Fig. 4.** The flextensional actuators are released from the laminate using a sequence of careful laser micromachining steps. The laminate before release (a) is first registered to the laser micromachining system, and then the linkage arms are formed (b), the piezoceramic edges cleaned (c), and the vias to the center layer machined (d). The vias are then filled with conductive epoxy (e) and the outer boundaries of the actuators are defined (f). For symmetry, these cuts are then repeated on the back side of the substrate. The released actuators are shown as a set (g), and a single actuator after cleaning and wiring is shown (h).

prepreg fibers. Sanding should be done on the bulk material before the individual pieces are formed. We find the medium roughness of papers from 240–600 grit to be appropriate. Third, small amounts of resin tend to squeeze out during lamination and build up on the edges of the stack. These can be sanded off before subsequent lamination steps. Lastly, some amount of resin will flow on top the copper layers during the final lamination step. This resin can also be removed with light sanding, or a two-ply copper can be used and the outer, resin-spotted layer peeled away to reveal a clean copper layer that is easy to solder to.

In the next fabrication step, the actuators are released from the laminate, which is shown before release in Fig. 4a. The process begins with the creation of the carbon fiber flexures and arms (b) using the same laser micromachining system described above. During this process, the vaporized carbon is deposited on the edges of the piezoceramic, which will lead to near instantaneous dielectric breakdown if not treated. To remedy this, we use the laser to remove these carbonized edges and create new, clean edges (c). With the laser-induced tapering in mind, these steps are undertaken symmetrically on the top and back sides, so as to ensure symmetry of the final device in the thickness direction. Next, trenches in the outer layers of carbon fiber and copper are formed to electrically isolate the connections to the different piezoelectric electrodes (d). Vias are also carefully cut through the alumina to the center carbon fiber layer, to allow electrical connection to the inner

electrodes. The vias are then filled with conductive epoxy, which connects to the previously formed copper pads (e). The final laser micromachining step is the definition of the outer border to fully release each actuator from the laminate (f). Once again, this cut is done symmetrically, from the top and back sides. The excess outer material can then be discarded to reveal the released actuators (g).

Post-processing, the final fabrication step, includes a few tedious but important processes. First, the edges of the piezoceramic should be cleaned with isopropyl-alcohol-wetted cloths to remove electrically conductive debris deposited during the release cuts. This is challenging due to the small space between the piezoceramic element and the carbon fiber arms, but it can be done using a thin cloth manipulated by tweezers. It would save processing time to use a batch cleaning process or to mask off the piezoceramic edges to sidestep the need for cleaning, and these directions would certainly merit investigation if large-scale production would be pursued. Second, the edges of the piezoceramic should be treated to enhance the dielectric strength of the actuators. For small batches of actuators we have used cyanoacrylate glue (Loctite 495) and individually coated the edges using a thin tungsten wire, but for larger batches, a parallelized process such as chemical vapor deposition of parylene could be used. Lastly, electrical connections to the actuators are made. The pads are lightly sanded, cleaned with flux remover, and tinned; similarly, thin copper wires are stripped and tinned.

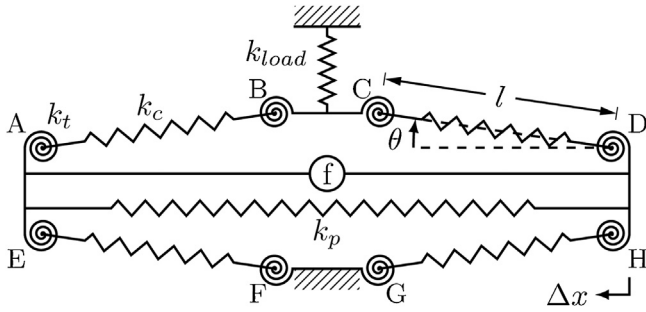


**Fig. 5.** Lumped parameter representation of the piezoelectric flextensional actuator. The piezoceramic transducer is represented by a voltage-dependent force source  $f$  in parallel with a prismatic spring  $k_p$ . The flexure hinges are represented by torsional springs with stiffness  $k_t$ , and the series equivalent stiffness of each set of flexure hinges and amplification arm is represented by the prismatic spring of stiffness  $k_c$ . This simplified model grants insight into proper sizing of the amplification frame stiffness relative to the piezoceramic stiffness.

The wires are then soldered to the pads to complete the electrical connections.

#### 4. Modeling

Analytic prediction of absolute performance of flextensional actuators is a complex modeling problem that has attracted many different approaches. To contextualize and motivate our approach, a brief examination of these methods is warranted. The simplest approach is the equivalent rigid body method, in which the torsional stiffness of the flexures and bending stiffness of the connecting arms are lumped into torsional stiffnesses acting about ideal revolute joints [7]. The next step in complexity is to treat the flexures and arms as discrete Euler-Bernoulli beams. This is the approach of Wei et al. [15], who analyzed the general case of a compliant bridge-type mechanism and provided analytic solutions for their deformation under applied force. That approach was generalized by Ling et al. [13], so as to cover a broader class of planar compliant mechanisms and to include the dynamics of the structure. Liu et al. [9] used a matrix-based approach to find the equivalent compliance of the flexures at the input and output links. All of these methods discretize the structure in a way that lets the mechanism be represented with some minimal degrees of freedom. The goal of such efforts is to provide general insight to the designer without resorting to finite element analysis.

Two key themes that emerge from these modeling efforts are the sensitivity of device performance to flexure hinge width and the sensitivity of analytical models at high displacement amplification ratios. In the section that follows, we strip away most of the modeling complexity and distill these insights into quantitative design guidelines that allow a designer to size the flexure hinge width for a particular piezoelectric force and linkage amplification ratio. Unlike any of the more complex methods previously proposed, our approach does not require significant algebra, solving equations of static equilibrium, and the like. This should be particularly useful for those who prefer a model-light, design-by-experiments approach, for whom a loss in modeling accuracy can be compensated for with the information gained from experimental measurements.

##### 4.1. Lumped parameter modeling

With a view toward simple design guidelines, we use the equivalent rigid body approach, with the parameters and geometric definitions shown in Figs. 1 and 5. The analysis will proceed by addressing the two extreme cases of actuator behavior: free displacement and blocked force. This allows the effects of the torsional stiffness  $k_t$  of the flexures and the compressive stiffness  $k_c$  of the

linkage to be treated separately, simplifying the analysis. In the free displacement case, the torsional stiffnesses dominate, and in the blocked force case, the compressive stiffnesses dominate.

First, in the free displacement case, the torsional stiffnesses  $k_t$  of the flexure hinges are reflected back to the active element. The equivalent energy  $U$  stored in the eight flexures is equivalent to that stored in a single linear spring in parallel with the active element, as given by:

$$U = 8 \left( \frac{1}{2} k_t \Delta \theta^2 \right) = \frac{1}{2} k_{eq,t} \Delta x_p^2 \quad (1)$$

where  $k_{eq,t}$  is the equivalent stiffness seen by the active element and  $\Delta x_p = 2\Delta x$  is the active element's displacement. Assuming small deviations from the initial configuration, it follows from geometry that  $\Delta x = l\Delta\theta \sin\theta$ . Substituting this into (1), the equivalent stiffness  $k_{eq,t}$  is found to be:

$$k_{eq,t} = \frac{2k_t}{l^2 \sin^2(\theta)} \quad (2)$$

Second, in the blocked force case, the compressive stiffness of the flexures and linkage arms, together represented by the lumped parameter  $k_c$ , are reflected back to the active element. The energy stored in the four linkage arms and flexures  $U$  is equivalent to that stored in a single spring in parallel with the active element, as given by:

$$U = 4 \left( \frac{1}{2} k_c \Delta l^2 \right) = \frac{1}{2} k_{eq,c} \Delta x_p^2 \quad (3)$$

Assuming small displacements of the structure, for this case it follows from geometry that  $\Delta x = \Delta l \cos\theta$ . These terms can be substituted into (3) to yield the following expression for the equivalent stiffness  $k_{eq,c}$ :

$$k_{eq,c} = \frac{k_c}{\cos^2(\theta)} \quad (4)$$

In the free displacement case, the motion of the active element is reduced by the factor  $\eta_u$ , termed "displacement efficiency" due to the parallel stiffness of the torsional hinges, such that:

$$\eta_u = \frac{k_p}{k_p + k_{eq,t}} = \frac{1}{1 + k_{eq,t}/k_p} \quad (5)$$

Similarly, in the blocked force case, any motion of the active element represents a reduction in the actuator's output force. The displacement of the active element  $\Delta x_p$  is given by:

$$\Delta x_p = f_p / (k_p + k_{eq,c}) \quad (6)$$

"Force efficiency",  $\eta_f$ , the fraction of the active element force that contributes to the output force of the actuator, can be written as:

$$\eta_f = 1 - \frac{\Delta x_p}{u_p} = \frac{k_{eq,c}}{k_p + k_{eq,c}} = \frac{1}{1 + k_p/k_{eq,c}} \quad (7)$$

where  $u_p = f_p/k_p$  is the free displacement of the active element.

The actuator's output characteristics can now be written as a function of the active element properties and the linkage lumped parameters. First, the actuator's free displacement  $u_a$  is given to be:

$$u_a = \eta_u T u_p \quad (8)$$

where  $T$ , the geometric transmission ratio from the active element to output link motion is simply given by  $T = \cot\theta$  and  $u_p$  is the active element's free displacement. Second, the actuator blocked force  $f_a$  can be written as:

$$f_a = \eta_f \frac{f_p}{T} \quad (9)$$

Now we are prepared to write the actuator's mechanical efficiency in terms of the quantities defined above. For any actuator

formed from an active element acting through a flexible transmission, the mechanical efficiency  $\eta_{mech}$  can be written as:

$$\eta_{mech} = \frac{u_a f_a}{u_p f_p} \quad (10)$$

Clearly, this represents the reduction in energy output of the actuator from that of the active material. Substituting from above, we find that mechanical efficiency can be recast as;

$$\eta_{mech} = \eta_u \eta_f \quad (11)$$

#### 4.2. Scaling analysis and design guideline derivation

Now we are prepared to use the lumped parameter model to derive design guidelines for choosing geometric and material parameters. Given some minimum desired displacement and force efficiencies  $\eta_{u,des}$  and  $\eta_{f,des}$ , respectively, two design constraints can be written using the relations above:

$$k_{eq,t} < 2k_p \left( \frac{1 - \eta_{u,des}}{\eta_{u,des}} \right) \quad (12)$$

$$k_{eq,c} > k_p \left( \frac{\eta_{f,des}}{1 - \eta_{f,des}} \right) \quad (13)$$

where the factor of two accounts for the strain stiffening of the piezoceramic, as described in [12].

We can employ the simplest torsional stiffness model for the flexure hinges, that of an Euler-Bernoulli beam:

$$k_t = 2 \left( \frac{Y_f t_f w_f^3}{12 l_f} \right) \quad (14)$$

The factor of two accounts for the double flexure of the parallelogram design. Under this definition we implicitly assume that the linkage arms are rigid and that all rotation occurs in the flexures. Then, by taking the centers of rotation of the flexure hinges to be fixed at the hinge centers, the distance between the centers  $l$  from Fig. 5 becomes:  $l = l_l + l_f$ . Note that more sophisticated representations of flexure stiffness could be inserted here in accordance with different kinematic assumptions and/or choices of flexure geometry.

The lumped stiffness  $k_c$  can similarly be written in terms of geometric and material properties:

$$k_c = 2 \left( \frac{k_f k_l}{k_f + 2k_l} \right) = 2 Y_f t_f \frac{w_f w_l}{w_f l_l + 2 w_l l_f} \quad (15)$$

where  $k_f$  and  $k_l$  are the compressive stiffnesses of a single flexure and arm, respectively, and the factor of two accounts for the parallelogram structure. Note that we assume that the flexure and arm are constituted of the same material and thickness. In the same way, the stiffness of the piezoceramic element can be written simply as:

$$k_p = Y_p w_p t_p / l_p \quad (16)$$

where  $Y_p$  represents the elastic modulus in the zero strain condition.

Now, substitutions can be made to express the design constraints (12 and 13) in terms of the material properties and geometric parameters. Two cases will be considered: first, the general case in which the designer is free to choose all parameters, and second, a more restricted case in which order of magnitude assumptions are used to reduce the dimensionality of the design space to the most critical subset of design choices.

##### 4.2.1. General case

When all parameters are left free to the designer, the design constraints take the form:

$$\frac{1}{6} \frac{Y_f t_f w_f^3 l_p}{Y_p t_p w_p l_f} \frac{1}{(l_l + l_f)^2 \sin^2 \theta} \left( \frac{\eta_{u,des}}{1 - \eta_{u,des}} \right) < 1 \quad (17)$$

$$2 \frac{Y_f t_f l_p}{Y_p t_p w_p} \frac{w_f w_l}{w_f l_l + 2 w_l l_f} \frac{1}{\cos^2 \theta} \left( \frac{1 - \eta_{f,des}}{\eta_{f,des}} \right) > 1 \quad (18)$$

A few trends can be identified. Decreasing the flexure width  $w_f$  will more quickly satisfy (17) than violate (18), so all things being equal, flexure width should be decreased in order to satisfy the constraints. This is particularly necessary for small angles of  $\theta$ , at which (17) becomes increasingly difficult to satisfy. Correspondingly, at high angles of  $\theta$ , the designer is free to choose a wider flexure. Lastly, note that at some small angles of  $\theta$  it is likely that no feasible choice of material properties and geometric parameters will satisfy both constraints.

##### 4.2.2. Simplified case

The designer can make scaling assumptions for their specific design problem in order to cast (17 and 18) into more simplified forms. These assumptions can be drawn from manufacturing constraints and geometric scaling between parameters. A set of scaling assumptions for the millimeter-sized actuators described herein might be as follows:

- 1 *Constant thickness.* From the manufacturing process used (Section 3), large ratios between piezoceramic and frame thickness are difficult to achieve. We assume these to be nearly equal:  $t_p \approx t_f$ .
- 2 *Ratio-metric lengths.* To achieve reasonable absolute displacements, the linkage arms should be longer than the flexures. We can choose:  $l_l = 5 l_f$
- 3 *Ratio-metric lengths.* From geometric constraints, and assuming the length of the output link to be very small, it follows from the second assumption that:  $l_p = 14 l_l / 5$ .
- 4 *Localized rotation.* To ensure that bending primarily occurs in the flexure regions, the linkage arms should be much stiffer in bending than the flexures. Because the flexure and arm materials are the same, this means that:

$$\frac{l_f w_l^3}{l_l w_f^3} \gg 1 \quad (19)$$

By choosing  $w_l = 5 w_f$  we ensure that the linkage arms are 25× stiffer than the flexure regions.

These assumptions yield the following simplified constraints:

$$\frac{343}{27} \frac{Y_f w_f^3}{Y_p l_p^2 w_p} \frac{1}{\sin^2 \theta} \left( \frac{\eta_{u,des}}{1 - \eta_{u,des}} \right) < 1 \quad (20)$$





$$\frac{28}{3} \frac{Y_f w_f}{Y_p w_p} \frac{1}{\cos^2 \theta} \left( \frac{1 - \eta_{f,des}}{\eta_{f,des}} \right) > 1 \quad (21)$$

These relations should be useful in the scenario in which a designer is given a piezoceramic element, amplification frame material, and nominal transmission ratio and wants to select a flexure size without resorting to cumbersome modeling methods that require computing forces and displacements in the entire structure.

## 5. Results

The design enhancements described in Section 2 yield an increase in mechanical efficiency from 33% to 70% across four actuator generations as shown in Table 1. The first generation is the

**Table 1**  
Comparison of multiple generations of millimeter-sized piezoelectric flextensional actuators showing the increase in mechanical efficiency arising from the incorporation of alumina base connections, parallelogram amplification topology, and proper selection of flexure geometry across design generations.

		Gen. I [11]	Gen. II	Gen. III	Gen. IV
					
<b>Piezoceramic active element</b>					
Number		1	2	2	2
Length × width [mm]		8.00 × 0.43	7.40 × 0.41	7.44 × 0.425	7.44 × 0.425
Bridge length [mm]	$l_p, w_p$	0.4	0.3	0.28	0.28
Thickness [μm]	$t_p$	135	135	135	135
$d_{31}$ [pm V <sup>-1</sup> ] at 1.5 V μm <sup>-1</sup>		544	544	544	544
$f_{31,block}$ [Pa m V <sup>-1</sup> ] at 1.5 V μm <sup>-1</sup>		26	26	26	26
Free displacement [μm]	$u_p$	6.5	6.0	6.1	6.1
Blocked force [N]	$f_p$	2.26	4.32	4.48	4.48
Total active mass [mg]		3.62	6.39	6.66	6.66
<b>Amplification frame</b>					
Base connection		UD CF	Alumina	Alumina	Alumina
Topology		Single arm	Single arm	Parallelogram	Parallelogram
Flexure type		Circular	Corner-fillet	Corner-fillet	Corner-fillet
Linkage angle [°]	$\theta$	3.35	3.4	3.4	3.4
Flexure width [μm]	$w_f$	20	30/20	30	60
Flexure length [μm]	$l_f$	–	60/90	60	480
Flexure radius [μm]		140	–	–	–
Fillet radius [μm]		–	50	50	50
Arm width [μm]	$w_a$	490	560	340	350
Arm length [mm]	$l_i$	3500	3300	3300	2500
<b>Actuator performance</b>					
Free displacement [μm]	$u_a$	86	90.5	83.8	89.6
Blocked force [mN]	$f_a$	57	191	211	211
Mass [mg]		7.6	16.0	17.5	16.8
Bandwidth [kHz]		–	1.6	–	2.1
<b>Performance metrics</b>					
Mass efficiency [%]	$\eta_{mass}$	48	40	38	40
Mechanical efficiency [%]	$\eta_{mech}$	33	66	65	70
Displacement efficiency [%]	$\eta_u$	74	89	82	88
Force efficiency [%]	$\eta_f$	42	75	79	79

base design described in prior work [11], in which a single piezoceramic beam is held inside a unidirectional carbon fiber frame. The second generation design uses two piezoceramic active elements and incorporates the alumina base attachments. The third generation is similar to the second, except the amplification arms are split into the parallelogram structure that reduces the serial compliance seen between the active element and the load. The fourth generation is similar to the third, except the flexure geometry is chosen in accordance with the scaling analysis conducted in Section 4.2. The target efficiencies were  $\eta_{u,des}=76\%$  and  $\eta_{f,des}=91\%$ , chosen somewhat arbitrarily to simulate a real design scenario, and the achieved efficiencies were 88% and 79%, respectively. This small deviation is likely due to some small unmodeled compliance in the frame and uncertainty in the material parameters.

The most significant trend that can be seen is an increase in blocked force from generation to generation while free displacement stays relatively constant. The second through fourth generations, which employ two active elements and alumina base attachments, all have significantly higher blocked force than the first generation. The small differences in blocked force and free displacement seen in the second through fourth generations are due primarily to different flexure geometry and amplification frame topology and in part to the slightly larger active elements employed.

To elucidate these trends and provide clarity to the derived values, a detailed description of the tabulated figures is merited. First, the length and width of the active elements and the linkage geometry were measured using a confocal microscope (Olympus OLS 4000). The measured values were largely as designed, with some small variations due to the evolution and refinement of the manufacturing process. Inadvertently, half of the flexures on the second generation device were made slightly elongated from the

others, which was resolved for subsequent generations. The active element thickness was simply measured using a micrometer. The piezoelectric coefficients  $d_{31}$  and  $f_{31,block}$  were taken from previous experimental work [12]. Note that these values are significantly higher than typical values reported by manufacturers, which are given for low field operation. The free displacement  $u_p$  and blocked force  $F_p$  of the active element were calculated from its geometry and material model, i.e.:

$$u_p = d_{31}El_p \quad (22)$$

$$F_p = f_{31,block}Et_pw_p \quad (23)$$

where  $E$ , the applied electric field, is 1.5 V μm<sup>-1</sup> for all tabulated values. For the first generation, data is as reported in [11]. For the second through fourth generations, free displacement was measured using a high-zoom inspection camera (PixeLINK PL-B741F), with resolution of 1.6, 2.77, and 2.4 μm/pixel for the respective measurements. Blocked force was measured using a load cell (ATI Nano17 Titanium) with a resolution of 1.5 mN. The actuators were weighed using an electrobalance (Cahn 25). Lastly, bandwidth, defined as the  $f_{-3dB}$  frequency, was measured using a laser Doppler vibrometer (Polytec PSV-500).

Lastly, we conducted a series of experiments to validate the constancy of the output stiffness across a range of load stiffnesses and operating conditions. Springs of various stiffness were placed between the load cell and the output link of the actuator, and output force and displacement were measured simultaneously (displacement was measured with the inspection camera, as before). These experiments were conducted on a Generation III actuator. The results are shown in Fig. 6, and it can be seen that output stiffness is nearly constant at  $\sim 2.75$  N mm<sup>-1</sup>, with some nonlinear effects becoming visible at high fields.



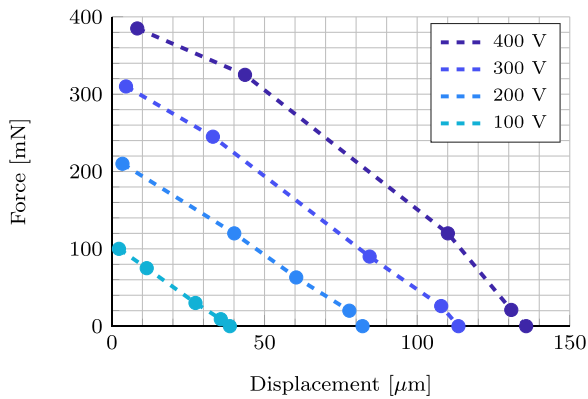


**Fig. 6.** Static performance of the Generation III design with a purely compliant load, across a range of input voltages and load stiffnesses. Output stiffness is nearly constant at low fields and varies slightly at high fields. A maximum energy density of  $1.5 \text{ J kg}^{-1}$  is achieved at 400 V.

## 6. Discussion

The millimeter-sized flextensional actuators described herein compare favorably to existing centimeter-sized designs. The most mechanically efficient actuator seen in the literature is that of Janker et al. [6]. Their centimeter-scale actuator uses an aluminum frame with the parallelogram topology and achieves 83% mechanical efficiency at 33% mass efficiency, compared to 70% mechanical efficiency and 40% mass efficiency for the Generation IV actuator.

The actuators presented in this work also compare favorably to other millimeter-sized piezoceramic actuator topologies. Of particular interest are bimorph bending actuators, which are widely used in microrobotic devices. For a similarly sized bimorph beam ( $L \times W = 8.2 \text{ mm} \times 2 \text{ mm}$ ), the free displacement and blocked force of the active element are  $6.7 \mu\text{m}$  and  $10.6 \text{ N}$ , respectively, and the free displacement and blocked force of the actuator are  $375 \mu\text{m}$  and  $115 \text{ mN}$ , respectively. This yields a mechanical efficiency of 61%. The mass efficiency is the mass of the active elements ( $34.6 \text{ mg}$ ) divided by the total mass ( $43 \text{ mg}$ ) – 80%. Thus, the energy density achievable with the flextensional actuators is about 60% of the energy density of bimorphs. This could perhaps be further increased through incorporation of lighter passive materials and more exacting design optimization.

One difference between the actuators described herein and their centimeter-scale counterparts is our use of carbon fiber composites, where larger designs typically use spring steel or aluminum. The advantages of carbon fiber on the millimeter scale are twofold: (1) it can be laser-micromachined without a significant heat affected zone (and therefore experience minimal change in mechanical properties), and (2) it has a large specific modulus, which is important for microrobotic applications in which weight is a concern. Metals experience a heat-affected zone that becomes more and more significant the smaller the flexure becomes. The heat effect of melting and recast embrittles the material, which reduces the effectiveness of the flexure. It is possible that this heat effect could be reduced through careful process parameter selection, post-annealing, or clever manufacturing techniques, and we expect this to be an interesting topic of future research.

The most deficient aspect of these actuators is their dependence on the mechanical bridges to transfer force from the active element to the amplification frame. The bridges are in tension, and, while they are much stiffer than the piezoceramic elements, their bonds to the frame and piezoceramic, respectively, must be able to resist the shear force generated by the contracting piezoceramic. Unfortunately, it is difficult to guarantee high quality bonds due to the small bond area and variable quality of prepreg carbon fiber. A bet-

ter approach might be to prestretch the amplification frame around the active element, such that it always is in compression. In such a scheme, contraction of the active element would work to relieve the tension in the frame. Importantly, force transfer would no longer rely on the quality of the mechanical bridges. Also, in this scheme, a single piezoceramic element could be used instead of the two elements per actuator required herein, which would further simplify the assembly process. One trade-off of using a thicker piezoceramic would be the need for larger voltages to achieve equivalent electric fields, which could be a concern in embedded applications.

One component that this work does not significantly address is that of flexure hinge geometry selection, which is a complex subject unto itself. There is a rich literature on this topic [16–20] in which the mechanics of these hinges are considered and important properties such as rotation center stability and compliance ratios are derived. We used simple corner-filletted flexure hinges here but expect that further increase in device performance could be accrued through clever selection of flexure hinge geometry. Along these lines, the lumped-parameter-based scaling could be adapted to incorporate more sophisticated representations of rotational stiffness beyond the beam-bending approach taken here. This would increase the accuracy for specific device configurations, at the expense of making the design trends less visible. Note that despite employing corner-filletted flexure hinges we ignored the effect of the fillet in our modeling. For the geometry chosen for the Gen. IV actuator, this results in around 10% deviation in rotational stiffness from the model of [16], which we consider to be a small enough error to allow the use of the simpler model.

## 7. Conclusion

We have herein described a series of new flextensional millimeter-sized piezoceramic actuator designs with high mechanical efficiency (70%) and energy density ( $1.5 \text{ J kg}^{-1}$ ). Mechanical efficiency is an important quality metric, as it captures how well the flexible transmission converts the input work to output work. We have shown that to optimize mechanical efficiency it is useful to think in terms of equivalent stiffnesses, and that by focusing on the extremes of actuator behavior – blocked force and free displacement – the analysis can be simplified and simple design guidelines can be derived with the assistance of simple scaling assumptions. These devices expand the possibilities for millimeter-sized mechatronic devices, and the methods proposed should be broadly useful for designers of similar devices across all scales.

## Author contributions

Peter York: Conceptualization, methodology, investigation, writing – original draft. Noah Jafferis: Validation, writing – review & editing. Robert Wood: Supervision, funding acquisition, writing – review & editing.

## Conflict of interest

The authors declare that there is no conflict of interest.

## Acknowledgements

This work was funded in part by the DARPA SHRIMP program (award number HR0011-19-C-0044), the National Science Foundation (award number CMMI-1830291), and the Wyss Institute for Biologically Inspired Engineering. Any opinions, findings, and conclusions or recommendations expressed in this material are those of the authors and do not necessarily reflect the views of the National Science Foundation or DARPA.

## References

- [1] K.D. Rolt, History of the flextensional electroacoustic transducer, *J. Acoust. Soc. Am.* 87 (3) (1990) 1340–1349.
- [2] R. Wood, E. Steltz, R. Fearing, Optimal energy density piezoelectric bending actuators, *Sens. Actuators A: Phys.* 119 (2) (2005) 476–488.
- [3] N.T. Jafferis, E.F. Helbling, M. Karpelson, R.J. Wood, Untethered flight of an insect-sized flapping-wing microscale aerial vehicle, *Nature* 570 (7762) (2019) 491.
- [4] X. Yang, Y. Chen, L. Chang, A.A. Calderón, N.O. Pérez-Arancibia, Bee+: a 95-mg four-winged insect-scale flying robot driven by twinned unimorph actuators, *IEEE Robot. Autom. Lett.* 4 (4) (2019) 4270–4277.
- [5] F. Claeysen, R.L. Letty, F. Barillot, O. Sosnicki, Amplified piezoelectric actuators: static & dynamic applications, *Ferroelectrics* 351 (1) (2007) 3–14.
- [6] P. Jänker, M. Christmann, F. Hermlé, T. Lorkowski, S. Storm, Mechatronics using piezoelectric actuators, *J. Eur. Ceram. Soc.* 19 (6) (1999) 1127–1131.
- [7] M.N.M. Zubir, B. Shirinzadeh, Y. Tian, Development of a novel flexure-based microgripper for high precision micro-object manipulation, *Sens. Actuators A: Phys.* 150 (2) (2009) 257–266.
- [8] J. Feenstra, J. Granstrom, H. Sodano, Energy harvesting through a backpack employing a mechanically amplified piezoelectric stack, *Mech. Syst. Signal Process.* 22 (3) (2008) 721–734.
- [9] P. Liu, P. Yan, Z. Zhang, Design and analysis of an x-y parallel nanopositioner supporting large-stroke servomechanism, *Proc. Inst. Mech. Eng. C: J. Mech. Eng. Sci.* 229 (2) (2015) 364–376.
- [10] H.-J. Lee, H.-C. Kim, H.-Y. Kim, D.-G. Gweon, Optimal design and experiment of a three-axis out-of-plane nano positioning stage using a new compact bridge-type displacement amplifier, *Rev. Sci. Instrum.* 84 (11) (2013) 115103.
- [11] P.A. York, N.T. Jafferis, R.J. Wood, Meso scale flextensional piezoelectric actuators, *Smart Mater. Struct.* 27 (1) (2017) 15008.
- [12] N.T. Jafferis, M.J. Smith, R.J. Wood, Design and manufacturing rules for maximizing the performance of polycrystalline piezoelectric bending actuators, *Smart Mater. Struct.* 24 (6) (2015) 65023.
- [13] M. Ling, J. Cao, Z. Jiang, J. Lin, A semi-analytical modeling method for the static and dynamic analysis of complex compliant mechanism, *Precis. Eng.* 52 (2018) 64–72.
- [14] Q. Xu, Y. Li, Analytical modeling, optimization and testing of a compound bridge-type compliant displacement amplifier, *Mech. Mach. Theory* 46 (2) (2011) 183–200.
- [15] H. Wei, B. Shirinzadeh, W. Li, L. Clark, J. Pinskiér, Y. Wang, Development of piezo-driven compliant bridge mechanisms: general analytical equations and optimization of displacement amplification, *Micromachines* 8 (8) (2017) 238.
- [16] N. Lobontiu, *Compliant Mechanisms: Design of Flexure Hinges*, CRC Press, 2002.
- [17] S. Zelenika, M.G. Munteanu, F. De Bona, Optimized flexural hinge shapes for microsystems and high-precision applications, *Mech. Mach. Theory* 44 (10) (2009) 1826–1839.
- [18] P.P. Valentini, E. Pennestrì, Elasto-kinematic comparison of flexure hinges undergoing large displacement, *Mech. Mach. Theory* 110 (2017) 50–60.
- [19] U. Hanke, E.-C. Lovasz, M. Zichner, N. Modler, A. Comsa, K.-H. Modler, Synthesis of PR/RP-chain based compliant mechanisms: design of applications exploiting fibre reinforced material characteristics, *New Trends in Mechanism and Machine Science* (2015) 743–751.
- [20] S. Linß, P. Gräser, T. Räder, S. Henning, R. Theska, L. Zentner, Influence of geometric scaling on the elasto-kinematic properties of flexure hinges and compliant mechanisms, *Mech. Mach. Theory* 125 (2018) 220–239.

## Biographies



**Peter A. York** is a Ph.D. Candidate in the Harvard Microrobotics Lab. He received his B.E. in Mechanical Engineering from Vanderbilt University in 2014 and is a recipient of the NSF Graduate Research Fellowship. His research interests include millimeter-scale fabrication, processing of smart materials and composites, electrostatic and piezoelectric actuators, and medical robotics.



**Noah T. Jafferis** obtained his Ph.D. in Electrical Engineering at Princeton University in 2012, and is currently a Postdoctoral Research Associate in Harvard University's Microrobotics Lab. Noah was home-schooled until entering Yale University at the age of 16, where he received his B.S. in Electrical Engineering in 2005. His research has included printing silicon from nanoparticles; traveling-wave propulsion of thin sheets; flapping-wing vehicle design and system optimization; piezoelectric actuators, motors, and thrusters; solar power for insect-scale robots; and self-sensing actuation. Noah's current research interests include micro/nano-robotics, bio-inspired engineering, 3D integrated circuits, MEMS/NEMS, piezoelectrics, 3D printing, energy harvesting, and large-area/flexible electronics.



**Robert J. Wood** (F'19) received the M.S. and Ph.D. degrees from the Department of Electrical Engineering and Computer Sciences, University of California, Berkeley, in 2001 and 2004, respectively. He is currently the Charles River Professor of Engineering and Applied Sciences at the Harvard John A. Paulson School of Engineering and Applied Sciences. His current research interests include micro-robotics, soft material robots, and bio-inspired robotics.